



# Identifying Complex Dynamics of Interacting Turbulent Jets through Modal Decompositions

Michael A. Meehan\*, Nicholas T. Wimer†

*Department of Mechanical Engineering, University of Colorado, Boulder, CO*

Ankit Tyagi,‡ Jacqueline O'Connor§

*Department of Mechanical Engineering, The Pennsylvania State University, University Park, PA*

Peter E. Hamlington¶

*Department of Mechanical Engineering, University of Colorado, Boulder, CO*

**The interaction of initially isolated jets arises in a wide range of engineering applications, including cooling devices, combustors, and fuel injectors. Many previous investigations of such applications have focused primarily on how the jet interactions affect time-averaged flow and turbulence characteristics. However, the dynamical processes underlying these interactions have remained largely unexplored, leading to potential uncertainty regarding the performance and optimization of engineering systems. In this study, we explore interacting jet dynamics through highly resolved simulations of two turbulent interacting slot jets. We use adaptive mesh refinement to add resolution to the simulations only in the regions of interest. We perform proper orthogonal decomposition and dynamic mode decomposition on the region where the four shear layers associated with the initially separate jets merge and transition into a single jet stream. These decompositions allow us to distinguish between the different types of vortex shedding that occur, as well as to demonstrate the irregularity of the jet merging process.**

## I. Introduction

In a wide range of engineering and industrial systems, including aircraft engines, air curtains, ventilation systems, fuel injection systems, and stationary gas turbine combustors, interactions between multiple flow streams are observed. Optimization of such systems (for example, to increase efficiency or decrease pollutant formation in engines) critically relies on understanding the role played by these interactions in the development of the flow. Moreover, in order to have predictive simulation capabilities, the fundamental properties of the underlying fluid dynamical processes must be accurately modeled.

The characteristics of axisymmetric, isothermal jets have been explored by a vast number of researchers, and Bayly et al. [1] review some of the basic mechanisms that drive instability in free shear flows. The shear layers in a turbulent jet often grow spatially through vortex pairing [2] before decaying into turbulence. Crow and Champagne [3] found a preferred mode of oscillation for these vortices. Further downstream in this highly turbulent region, the jet exhibits self-similar characteristics with respect to the flow width and the average centerline velocity, even if buoyancy plays a role [4]. Much more discussion on this topic is given by Ball et al. [5].

In an effort to understand more practical systems, incorporating upstream turbulence is required to accurately represent the development of jet seen in these systems. Hussain and Zedan [6] showed that increasing the perturbation level of the boundary layer in an axisymmetric jet noticeably increases the initial shear layer width and growth. Adding boundary layer turbulence also diminishes the vortex pairing process [7]. To accurately simulate experiments with highly turbulent inlets, many modeling strategies have been devised and show good agreement with experiments [8]. Using direct numerical simulations, Stanley and Sarkar [9] showed that different turbulence generating mechanisms can significantly alter the vortex shedding process.

\*Research Assistant, Department of Mechanical Engineering, UCB 427, Boulder, CO, AIAA Student Member

†Research Assistant, Department of Mechanical Engineering, UCB 427, Boulder, CO, AIAA Student Member

‡Research Assistant, Mechanical Engineering, The Pennsylvania State University, AIAA Student Member

§Assistant Professor, Mechanical Engineering, The Pennsylvania State University, AIAA Senior Member

¶Assistant Professor, Department of Mechanical Engineering, UCB 427, Boulder, CO, AIAA Member

Far fewer studies have been performed to uncover the effects of interacting jets when the initial jets are in close proximity. For such configurations, the bulk streamwise motion in the flow field of unventilated parallel plane jets can be characterized by three regions; namely, the converging, merging, and combined regions (see Ko and Lau [10] for an illustration). The initial converging region ends when the mutual entrainment of each jet leads to a centerline velocity above zero; this downstream location is called the merge point and marks the beginning of the merging region. The fundamental vortex roll-up frequency is unaffected by the presence of the neighboring jet prior to the merge point [11], and only the turbulent stresses of the outer shear layers seem to be affected [10]. The flow continues to mix and develop, and eventually the velocity at the centerline reaches a maximum along the transverse direction. This point is termed the converged point. Locations further downstream are considered the combined region and where the flow exhibits a self-similar profile. Adjacent jets will increase the turbulent velocity fluctuations even in the combined region where the time-average profile resembles that of a single jet [12].

The spacing and velocities of the jets can dictate how the merging process unfolds. Yin et al. [13] found a simple trend in which increasing the Reynolds number or decreasing the separation between the jets substantially reduced the downstream distance at which the jets began to interfere with one another. A table outlining the many other experiments varying these parameters is found in Wang et al. [14]. Interestingly, Bunderson and Smith [15] found the phenomenon of flapping, in which the flow stream oscillates normal to the streamwise direction, and was able to control – and, ultimately, remove the existence of – the flapping by varying the momentum flux ratio between the jets. The jet with the lower velocity bends towards the higher speed jet, which impacts the locations of merging and converging [16]. This behavior has also been found in reacting jet flows [17]. Controlling the characteristics of the flowfield can also be achieved through acoustic excitation [11].

Interacting jets have also been studied in many other contexts besides the plane parallel configuration. Böhm et al. [18], Stein et al. [19], and Rieth et al. [20] performed numerical studies on opposed turbulent jets and found that simulating the flow inside the nozzle, while at the same time validating with experimental data, was the best strategy. No investigations to date have systemically varied turbulence levels in interacting plane parallel flows [21, 22]. Different arrays of interacting round jets lend themselves to a diverse set of flow development patterns [12, 23]. Additionally, increasing the temperature of the jets can impact the frequency of vortex shedding [24].

In all of these prior studies, most investigations have focused on how plane parallel jets affect the mean and turbulence characteristics compared to a single jet, and how varying spacing and inflow velocity affect the merging process. However, very few, if any, prior studies discuss the dynamical features that emerge as a result of the interactions between the jets. We seek to better understand the process by which the interacting jets merge through modal decompositions, particularly proper orthogonal decomposition (POD) and dynamic mode decomposition (DMD) [25].

POD was first introduced by Lumley [26] to the turbulence community as a means to extract coherent structures in chaotic turbulent flows. The advantage of POD lies in the fact that it decomposes a flow into a set of orthogonal basis functions that are optimal from an energy standpoint. This means that no other decomposition can outperform POD in terms of capturing the maximum amount of energy using a finite number of modes [27]. Thus, many investigations take advantage of this technique to identify large, energetic structures present in the flow and produce accurate reduced-order models from just a few POD modes. Several reviews have described the breadth of topics for which POD has been applied [28, 29].

DMD, first proposed by Schmid [30], has recently enabled a better understanding of temporal dynamics of each mode. An overview of the DMD algorithm used in this work is given in section III.B but, in brief, a linear mapping matrix is used to approximate how the flow transitions from one snapshot to the next, related to the Arnoldi method. In contrast to POD, DMD provides a more complete description of the dynamics because dynamic modes are orthogonal in time and temporally dictated by a single complex eigenvalue. The recent application of DMD to fluid dynamics has already resulted in new and valuable insights, as illustrated by Taira et al. [25].

The goal of the present work is to better understand the dynamical behavior of interacting jets as they merge through the use of these modal decompositions. The rest of the paper is organized as follows. In Section II, we explain our numerical procedure to simulate the interaction of two turbulent parallel slot jets. Following that, we discuss the methodology used to perform modal decompositions in Section III. Results are then presented in Section IV. Finally, we discuss conclusions and implications for future work in Section V.

## II. Description of Numerical Simulations

The numerical simulations outlined in this section were loosely based on the experimental configuration outlined in Tyagi et al. [17]. Although many of the flow properties were matched between the simulations and experiment,

the complex geometry of the experimental configuration was, however, not accounted for, thereby precluding direct comparisons of the simulations and experiments. Nevertheless, the present simulations are sufficient to allow application of POD and DMD techniques to the interacting jet problem, and future work will focus on a combined analysis of computational and experimental results.

### A. Governing Equations and Numerical Method

The numerical simulations were performed using PeLeLM, a second-order finite volume, low-Mach, adaptive mesh code [31]. In particular, this code solve the continuity, momentum, species, and enthalpy equations for a low-Mach flow given by

$$\frac{\partial \rho}{\partial t} + \frac{\partial(\rho u_i)}{\partial x_i} = 0, \quad (1)$$

$$\frac{\partial u_i}{\partial t} + u_j \frac{\partial u_i}{\partial x_j} = -\frac{1}{\rho} \frac{\partial p'}{\partial x_i} + \frac{1}{\rho} \frac{\partial}{\partial x_j} \left[ \mu \left( \frac{\partial u_i}{\partial x_j} + \frac{\partial u_j}{\partial x_i} - \frac{2}{3} \frac{\partial u_k}{\partial x_k} \right) \right], \quad (2)$$

$$\frac{\partial(\rho Y_m)}{\partial t} + \frac{\partial(\rho u_i Y_m)}{\partial x_i} = \frac{\partial}{\partial x_i} \left( \rho D_m \frac{\partial Y_m}{\partial x_i} \right) + \dot{\omega}_m, \quad (3)$$

$$\frac{\partial(\rho h)}{\partial t} + \frac{\partial(\rho u_i h)}{\partial x_i} = \frac{\partial}{\partial x_i} \left( \lambda \frac{\partial T}{\partial x_i} \right) + \sum_m \frac{\partial}{\partial x_i} \left( \rho h_m D_m \frac{\partial Y_m}{\partial x_i} \right), \quad (4)$$

on a series of nested, block-structured grids. No sub-grid scale model was used. In PeLeLM, the low-Mach formulation assumes a constant background pressure and a perturbational pressure from velocity fluctuations, and an ideal equation of state was imposed through the divergence constraint equation

$$\frac{\partial u_i}{\partial x_i} = \frac{1}{\rho c_p T} \left[ \frac{\partial}{\partial x_i} \left( \lambda \frac{\partial T}{\partial x_i} \right) + \sum_m \frac{\partial}{\partial x_i} \left( \rho h_m D_m \frac{\partial Y_m}{\partial x_i} \right) \right] + \frac{1}{\rho} \sum_m \left( \frac{\bar{W}}{W_m} - \frac{h_m}{c_p T} \right) \left[ \frac{\partial}{\partial x_i} \left( D_m \frac{\partial Y_m}{\partial x_i} + \dot{\omega}_m \right) \right]. \quad (5)$$

Here,  $\rho$  is the density,  $u_i$  are the velocity components,  $p'$  is the perturbational pressure,  $\mu$  is the dynamic viscosity,  $Y_m$  are the species mass fractions,  $D_m$  are the corresponding diffusivities,  $\dot{\omega}_m$  is the heat release rate for reactions,  $h$  is the enthalpy,  $T$  is the temperature,  $\lambda$  is the thermal diffusion,  $c_p$  is the specific heat, and  $W_m$  is the molecular weight of each species. Additional details of the equations and their formulation can be found in [32, 33].

On a single level, the numerical procedure for integration is as follows. We use a second-order Godunov procedure to predict the time-centered velocity on the cell faces by explicitly discretizing the convective terms and semi-implicitly solving for momentum diffusion [34]. We set the initial estimate for the thermodynamic variables equal to their current state. Next, we iteratively solve: (i) the advection velocity and thermodynamic fluxes,  $\rho h$  and  $\rho Y_m$ , applying the constraint from Eq. (5), (ii) face-centered, time-centered states for mass and energy, (iii) a multi-implicit spectral deferred correction [35] for species mass fractions, and (iv) a backward Euler type equation for time-advanced enthalpy. We only consider flows of air in these simulations, so reactions are neglected. We then compute the provisional time-averaged, cell-averaged velocity field. Finally, we update the perturbational pressure field and compute a final velocity. This simplified description of the solution algorithm can be found in much greater detail in [31].

The adaptive mesh refinement (AMR) in PeLeLM is achieved on an adaptive hierarchy of nested uniform grids. As the simulation evolves, cells are tagged for refinement based on user specified criteria, such as vorticity or density gradients. The regridding algorithm is called at a user-specified interval to dynamically refine the mesh by creating a series of independent, nested grids. The time-stepping procedure is most easily thought of as a recursive operation: (i) advance the current level in time, using boundary conditions from underlying grid as needed, (ii) advance the next finest level two time steps using the coarser level variables as boundary conditions, and (iii) synchronize between levels and interpolate corrections to the finer levels. Losses of conservation between levels is handled by averaging the fine data onto the coarse grid and through refluxing across the coarse/fine interface. More details on the procedure as well as complications that arise through the multi-grid approach are discussed in [36, 37].

### B. Physical and Computational Setup

Air at  $T = 301$  K is injected vertically into the bottom of a domain filled with quiescent air at  $T = 300$  K through three different areas: jets, small pilots, and big pilots. The two jets each have length  $L_j = 100$  mm and width  $W_j = 10$  mm and are separated by a center-to-center spacing  $S = 30$  mm, centered at  $y, z = 0$ . The four small pilots each span a

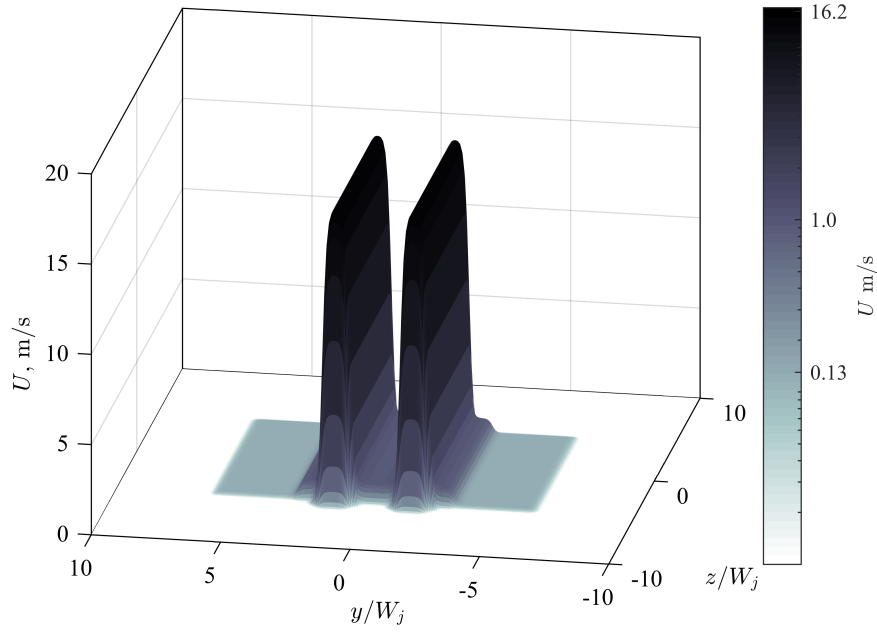


**Fig. 1** Surface plot of inlet profile at  $x = 0$  highlighting the three different regions: jet, small pilot, and big pilot flows.

length  $L_s = 89$  mm and width  $W_s = 10$  mm on both sides of each jet. On the outer edges of the small pilots, two big pilots, each with  $L_b = 90$  mm and  $W_b = 32$  mm, are positioned adjacent to the small pilots. Figure 1 illustrates the inlet velocity profile as a three-dimensional surface plot of the incoming streamwise velocity at  $x = 0$ . The mathematical implementation of the jet profile is given as

$$u_x = \frac{1}{4} \left[ \tanh\left(\frac{y + (S/2 + W_j/2)}{3W_j/20}\right) - \tanh\left(\frac{y + (S/2 - W_j/2)}{3W_j/20}\right) + \tanh\left(\frac{y - (S/2 - W_j/2)}{3W_j/20}\right) - \tanh\left(\frac{y - (S/2 + W_j/2)}{3W_j/20}\right) \right] \times \left[ \tanh\left(\frac{z - (L_j/2)}{3W_j/20}\right) - \tanh\left(\frac{z + (L_j/2)}{3W_j/20}\right) \right] + \text{perturbations} . \quad (6)$$

where similar expressions are used to specify the small and big pilot flows. The time-average velocities of jets, small pilots, and big pilots correspond to  $U_j = 16.2$  m/s,  $U_s = 1.0$  m/s,  $U_b = 0.13$  m/s, respectively, to match experimental mass flow rates. The background pressure field is hydrostatic and the total pressure is allowed to vary with velocity fluctuations, as discussed briefly in Section II.A.

The simulations are conducted in a  $0.2 \text{ m}^3$  domain on a base grid of  $128^3$  cells. This relatively large domain allows for proper entrainment and interaction between the two jets. All conditions on the inlet are Dirchlet boundary conditions and the other boundaries are outflow conditions to facilitate entrainment and departure of fluid. Three different simulations are conducted where only the maximum level of AMR is adjusted to 1, 2, or 3 or levels. These correspond to finest resolutions of  $\Delta x = 0.781, 0.391, 0.195$  mm, respectively.

As indicated in Eq. (6), perturbations were added to the jet inflow by generating fluctuating velocities in a  $0.01 \text{ m}^3$  domain with a wavenumber of  $k_0 = 6$  on a high resolution grid of  $512^3$ . This domain scale corresponds to the width of the jets and the wavenumber to the approximate radius of the holes generating turbulence inside the experiment. Coefficients of the wavenumber are downsampled such that wavenumbers that cannot be represented on our coarsest grid – approximately 12 grid cells across the inlet – are set to zero. The fluctuations are transformed into physical space then resampled on the number of cells that span the jet. The magnitude of the fluctuations was set to  $U_j/4$ . These fluctuations are then added to the bulk flow of the jets.

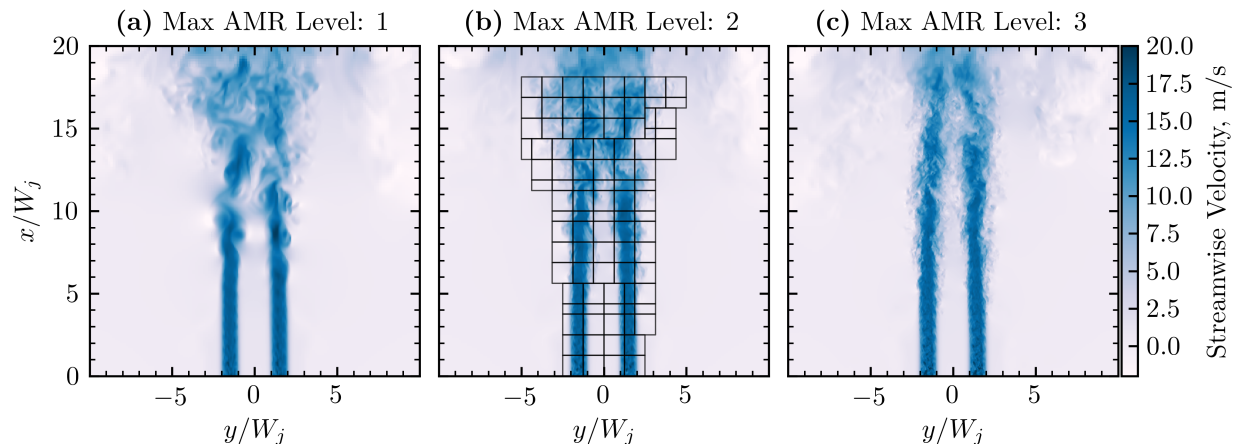


**Fig. 2** Instantaneous snapshots of the streamwise velocity from the simulations taken at the  $z = 0$  plane for (a) one level, (b) two levels, and (c) three levels of AMR. In (b), AMR grids of the finest level are shown to give the reader a sense of grid placement.

### C. Numerical Procedure using Adaptive Mesh Refinement

The primary regions of interest are the shear layer of the jets and where the jets begin to interact. The AMR capabilities in PeleLM enable us to resolve this particular region with the rest of the domain remaining coarse. This enhances the effective resolution in this dynamically complex region but keeps the computational expense tractable.

Many of the AMR parameters are tunable and thus, left to the discretion of the user to develop optimal criteria for numerical speed and efficiency. For these calculations, we tag cells for refinement with  $|\omega_i| > 3 \times 10^3$ , where  $\omega_i = \varepsilon_{ijk} \partial u_k / \partial x_j$  is the vorticity. Each successive level of refinement must be strictly contained within the next coarsest level (i.e., a region with the two levels of refinement must be surrounded by a region of one level of refinement). This ensures a smooth transition between the coarsest and finest levels. The number of buffer cells and size of grid on each level used in these simulations were found to produce satisfactory results within our computational budget.

In Figure 2, we present a centerline slice of streamwise velocity at  $z = 0$  with increasing levels of AMR, and we annotate the AMR grids in Figure 2b to give the reader a sense of grid placement. We can clearly see a difference in shear layer roll-up as our resolution increases. In the lowest resolution case at  $y/W \approx 8$ , all four shear layers show some coherent structures as vortices are first being formed, which distinctly contrasts the highest resolution case where more chaotic turbulent fluctuations seem to dominate this region. These processes do not seem to alter how and where the interaction zone begins. Quantitative results are presented in Section IV.

The results presented here come from extracted two-dimensional planes at  $z = 0$  at approximately equal time intervals of  $\Delta t = 1 \times 10^{-4}$  seconds, where velocity components are interpolated using a nearest-neighbor algorithm to a uniform grid of equal resolution to our finest AMR level. Meaning, since our base grid is  $128^3$ , for our finest resolution case we are interpolating all variables to a  $1024^3$  grid of equal dimensions. This process ensures there is no loss or enhancement (i.e., additional smoothness) when analyzing the AMR data. The time intervals of data collection in which the flow was fully developed for the three simulations were 0.2198, 0.1858, and 0.0234 seconds for the simulations with one level, two levels, and three levels of AMR, respectively.

## III. Modal Decomposition Techniques

Here we provide a brief overview of the methodologies used to perform POD and DMD, but direct the reader to the references for a more rigorous justification of each step in the process. This work has benefited greatly from the openness of other researchers in sharing the mathematical and algorithmic techniques to perform the decompositions described below.

In the following discussions on the methodology, we adopt the convention in which boldface capital letters refer to the matrix operator and lower case letters correspond to the vector components (or diagonal values of a diagonal matrix). For example, a series of  $N$  snapshots of the velocity field can be represented as  $\mathbf{U} = \mathbf{u}_1, \mathbf{u}_2, \dots, \mathbf{u}_N = \mathbf{u}_i$ .

### A. Proper Orthogonal Decomposition (POD)

POD provides a way to extract the major dynamical patterns in complex spatio-temporal dynamics through a series of snapshots of the flowfield. Typically, POD is applied to components of the fluctuating velocity fields to link the energy content to the turbulent kinetic energy, but can also be applied to scalar data, such as experimental data obtained using planar laser induced fluorescence (PLIF). We apply it here to the velocity data as these are readily available and provide the most meaningful results, as will be seen in section IV.

We choose to perform the POD using the method of snapshots as first proposed by Sirovich [38], because of its efficient algorithm when the number of spatial points  $M$  far exceeds the number of temporal snapshots  $N$ . First, the fluctuating velocity components are found by performing a Reynolds decomposition on the series of snapshots, namely

$$\mathbf{u}'(\mathbf{x}, t) = \mathbf{u}(\mathbf{x}, t) - \bar{\mathbf{u}}(\mathbf{x}). \quad (7)$$

All three fluctuating components are arranged into a single matrix  $\mathbf{U}(\mathbf{x}, t)$  with dimensions  $3M \times N$  because there are three velocity components [25]. The cross-correlation matrix is computed as  $\mathbf{C} = \mathbf{U}^T \mathbf{U} / (M - 1)$ , noting that with  $3M \gg N$ , the size of  $\mathbf{C}$  is significantly reduced compared to using other approaches, such as singular value decomposition. Next, the eigenvalue problem is solved on  $\mathbf{C}$ ,  $\mathbf{C}\Phi = \Lambda\Phi$ . The eigenvectors  $\phi_i$  are the basis functions, or POD modes, and are orthonormal, given by  $\langle \phi_i, \phi_j \rangle = \delta_{ij}$ , with  $\delta_{ij}$  as the Kronecker delta and  $\langle \cdot \rangle$  the inner product. The eigenvalues  $\lambda_i$  are the corresponding energies associated with each  $\phi_i$ , which are sorted such that  $\lambda_1 > \lambda_2 > \dots > \lambda_N$ . In other words, the first POD mode contains the greatest amount of energy and decreases for increasing mode number. Finally, the temporal coefficients are found by  $\mathbf{A} = \mathbf{C}^T \Phi$ , with the components  $a_i$  representing the temporal coefficients associated with each POD mode  $\phi_i$ . The flowfield can then be exactly represented by

$$\mathbf{u}(\mathbf{x}, t) = \bar{\mathbf{u}}(\mathbf{x}) + \sum_{i=1}^N a_i(t) \phi_i(\mathbf{x}). \quad (8)$$

Typically, the flow can be approximated with far fewer modes than  $N$ , but for this study, we discuss the dominant flow features extracted in each mode of the POD, so we do not specify a cut-off energy value for reconstruction.

### B. Dynamic Mode Decomposition (DMD)

DMD, first introduced to the fluid dynamics community by Schmid [30] and Rowley et al. [39], offers a more descriptive analysis of the dynamics of the decomposed modes. Rather than looking at the series of snapshots as a simple collection and calculating the maximum projection, as is done with POD, DMD attempts to describe the evolution between the snapshots through a linear map. This enables insights into the temporal dynamics in each mode.

We start the DMD analysis by reshaping the velocity data such that they are contained in a two-dimensional matrix  $\mathbf{U}$ , with the dimensions corresponding to space and time and containing all three velocity components. Next, two more data matrices are created that are almost identical to  $\mathbf{U}$ , except that the first new matrix  $\mathbf{X}$  drops the last snapshot and the second  $\mathbf{Y}$  drops the first snapshot.

The objective is to then minimize the error between  $\mathbf{X}$  and  $\mathbf{Y}$  through the linear mapping  $\tilde{\mathbf{A}}$ , meaning  $\mathbf{X} = \tilde{\mathbf{A}}\mathbf{Y}$ . Calculating  $\tilde{\mathbf{A}}$  explicitly is not efficient so we approximate it through the following algorithm.

The economic singular value decomposition is taken of  $\mathbf{X}$  to get the POD modes,  $\mathbf{U}$ , of  $\mathbf{X}$ , mathematically as  $\mathbf{X} = \mathbf{U}\Sigma\mathbf{V}^T$ . The tensor  $\tilde{\mathbf{A}}$  can be calculated by

$$\tilde{\mathbf{A}} = \mathbf{U}^T \mathbf{Y} \mathbf{V} \Sigma^{-1}. \quad (9)$$

To find the dynamic modes, the eigenvalue problem is solved on  $\tilde{\mathbf{A}}$  to find the eigenvalues  $\tilde{\mu}_i$  and eigenvectors  $\tilde{\mathbf{w}}_i$ . Note that since  $\tilde{\mathbf{A}}$  is not a positive symmetric matrix,  $\tilde{\mu}_i$  can be complex, and thus, can describe how the modes behave in time (e.g., growing, decaying, oscillating, etc.). The dynamic modes  $\psi_i$  and continuous eigenvalues  $\mu_i$  are computed by

$$\psi_i = \mathbf{U} \tilde{\mathbf{w}}_i, \quad \mu_i = \log(\tilde{\mu}_i) / \Delta t. \quad (10)$$

This methodology follows that of Schmid [30], but several other methodologies can also be used to arrive at the same answer (for example, see Kutz et al. [40]).

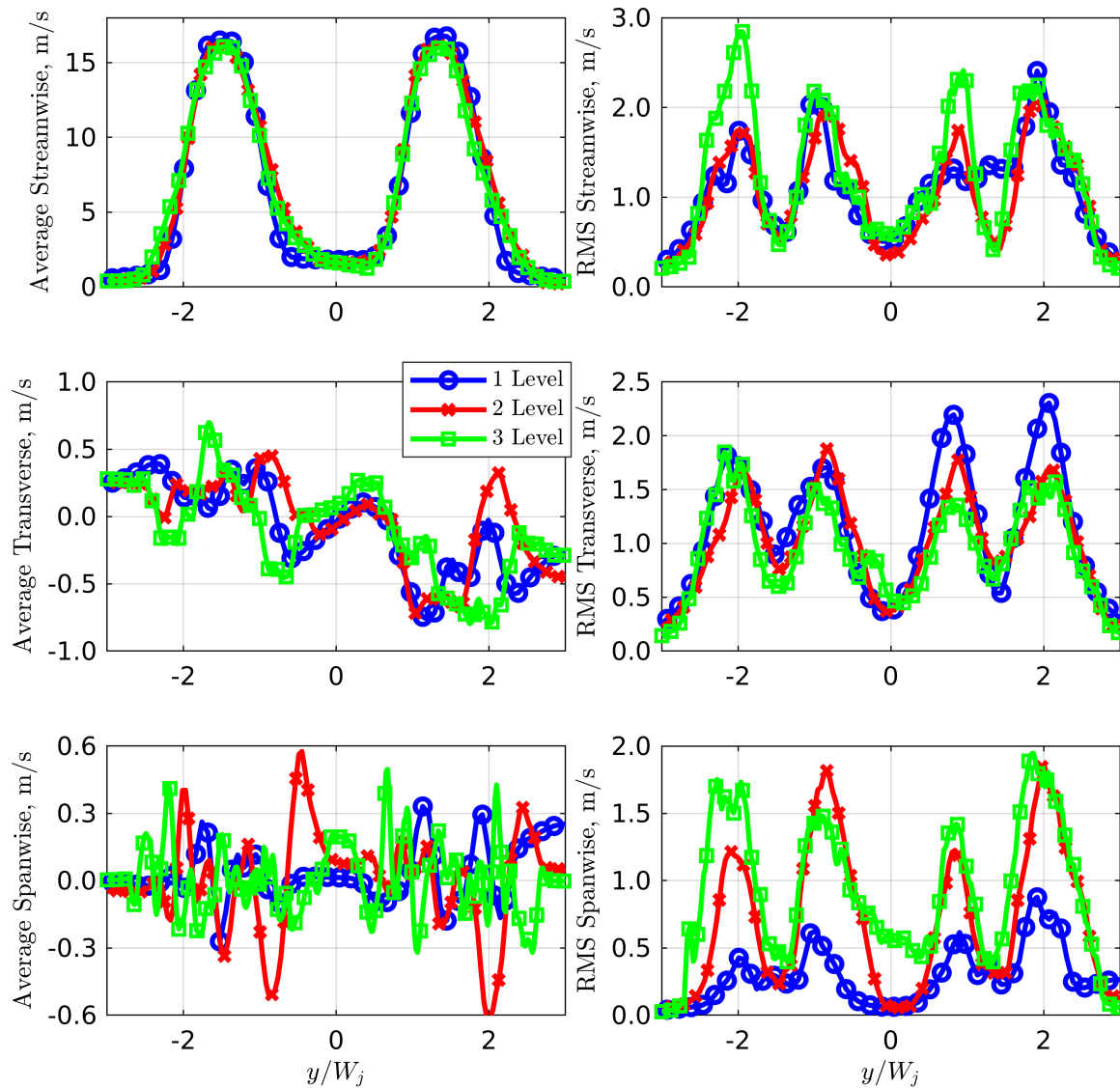


**Fig. 3** Comparison of time-average (left column) and RMS (right column) of the streamwise, transverse, and spanwise velocity components on the top, middle, and bottom rows, respectively, for a downstream location of  $x/W_j = 7$ .

#### IV. Results

We begin by comparing the time-average and RMS of the velocity components at a downstream location of  $x/W_j = 7$  in Figure 3 for the three different simulation resolutions. The streamwise velocity  $u_x$  shows a breakdown from the original top-hat profile initiated at the inlet as a result of shear layer growth. The tops of each profile are rounded and very little discrepancy exists between each resolution of simulation. The time-average transverse velocity  $u_y$  exhibits a slight asymmetry across  $y = 0$ , as we would expect due to different directions in which the shear layers of the jets are spreading. We attribute the slight difference in the two- and three-level simulations to the insufficient number of time steps in the three-level simulation. The spanwise velocity component  $u_z$  contains mostly random fluctuations about  $u_z = 0$  which is expected from the symmetry of the simulation.

The RMS fluctuations of each velocity component have similar profiles along the transverse direction because at this

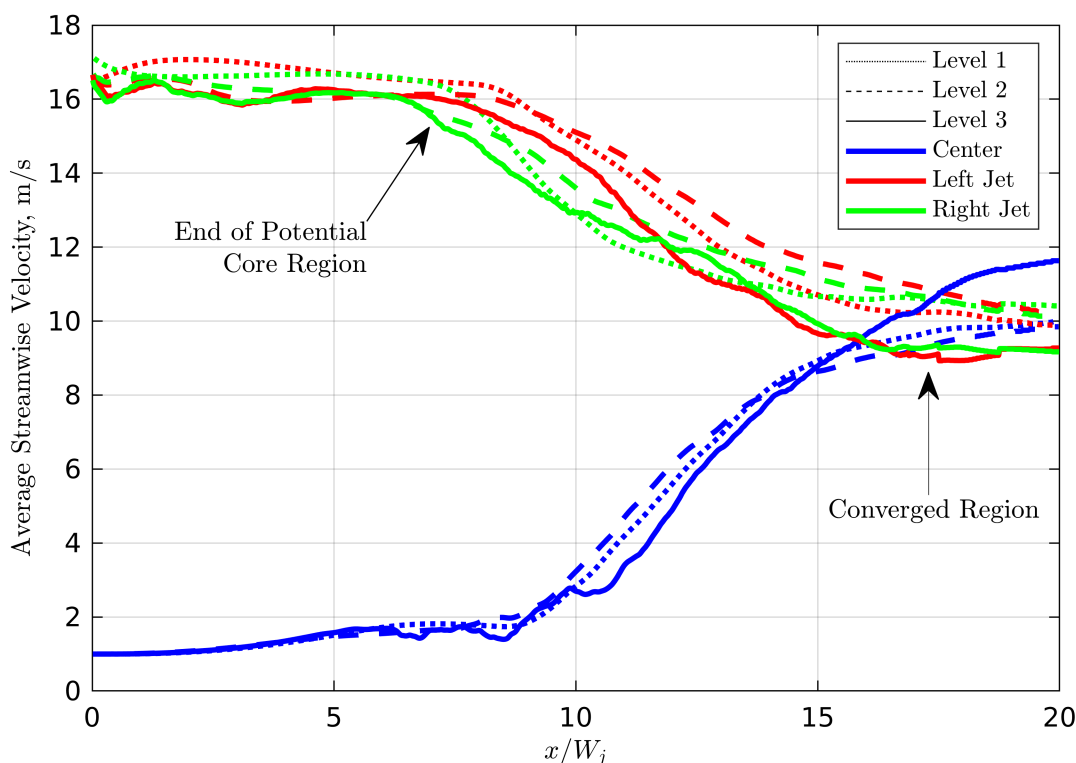


**Fig. 4** Average streamwise velocity as a function of downstream location at the centerline of the configurations  $y = 0$  and at the center of the jets  $y = -S/2, S/2$ .

downstream location, the large fluctuations are being produced along the shear layer. This particular location,  $x/W_j = 7$  illustrates the three-dimensionality of these fluctuations, since all three velocity components have similar orders of magnitude. Non-zero RMS values are observed at the center of the jets because the large turbulent fluctuations used as turbulent inflow persist downstream. The discrepancies between the two highest resolution cases are most likely due to a lack of snapshots of the highest resolution.

We also plot the time-average streamwise velocity profile at  $y = 0, -S/2, S/2$ , which corresponds to the centerline of the simulation and centerline of the jets, in Figure 4. We can see the potential cores of each jet persist until  $x/W_j \approx 6 - 7$ , and then as the jets continue to mix and interact, the centerline velocity becomes a maximum, marking the converging region, as discussed in Ko and Lau [10]. The jets break down fairly symmetrically and have similar behavior for each resolution of simulation. It would not be appropriate to comment, however, on the transition between converging and merging regions, since our simulations have a non-zero centerline velocity initiated at  $x = 0$ .

Next, we perform POD on the simulation with 2 levels of AMR using all three velocity components on the region  $x \in [75, 150]$  mm and  $y \in [-25, 25]$  mm. Figure 5 gives the spatial modes corresponding to the streamwise and transverse components in the top and middle rows, respectively, and the power spectral densities of the first four modes. The normalwise velocity is neglected because it did not have any recognizable structure. This particular region was chosen to highlight the interesting dynamics that occur as the jets begin to merge. Also, we do not show any results from performing POD on the three-level simulation because there was not enough data to resolve many of the features; however, the results (not shown here) seem to be tending towards those shown for two levels.

The four modes in Figure 5 show the transition at which the jets are shedding vortices along the four shear layer then farther downstream begin to merge and shed vortices asymmetrically about the centerline  $y = 0$ . Modes 3 and 4 have larger spatial fluctuations near the lower half of the POD domain. These two modes are termed a mode pair because they have almost identical energy content (not shown here) and power spectra, and spatial structures that appear 90 degrees out of phase with one another. Sets of these modes identify traveling structures in the flowfield. As the vortices represented by modes 3 and 4 travel downstream, their structure transforms into that of the more energetic modes 1 and

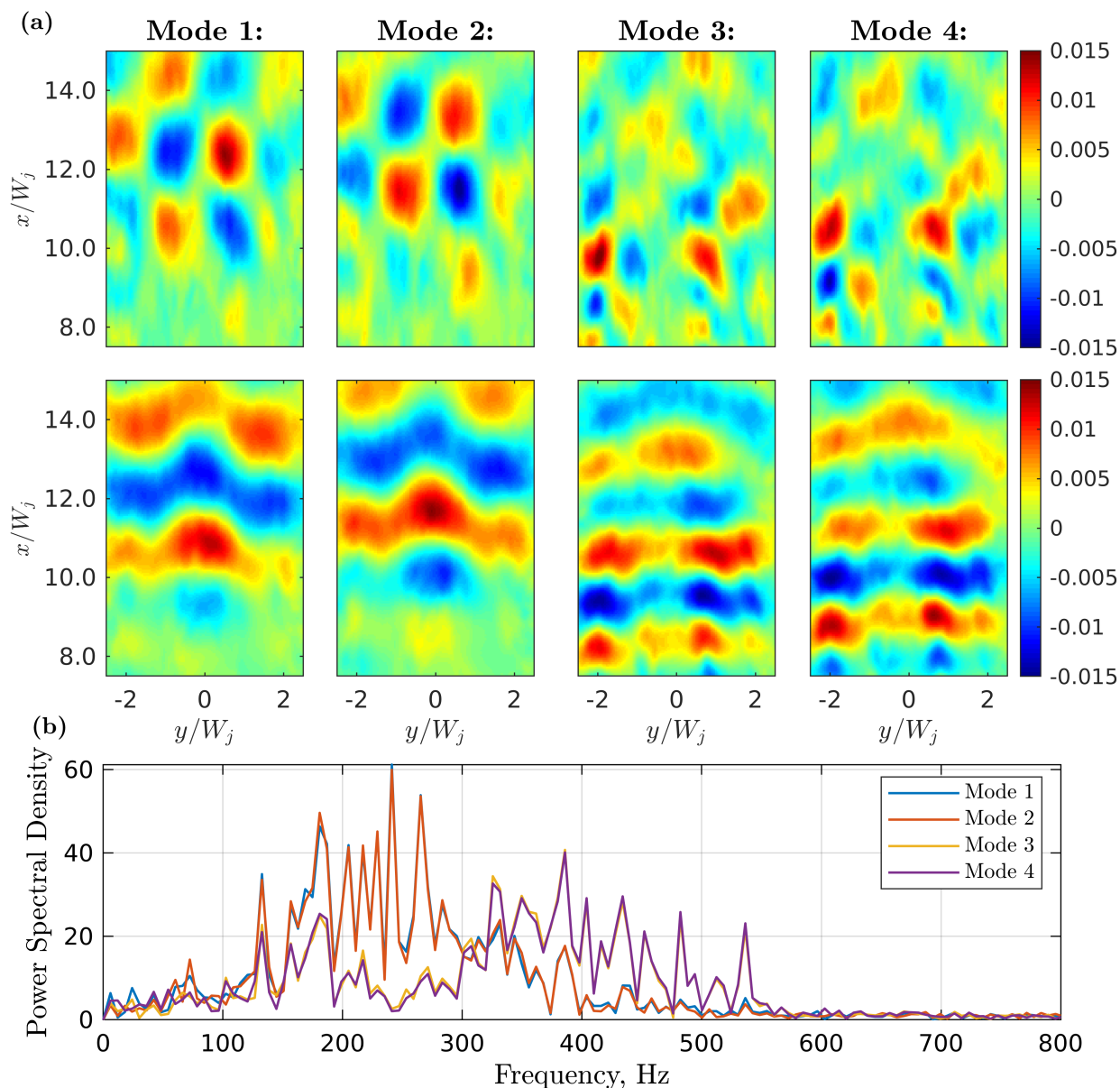


**Fig. 5** POD (a) spatial modes for the streamwise and transverse velocity components in rows 1 and 2 and (b) spectra of temporal coefficients computed for  $x \in [75, 150]$  mm and  $y \in [-25, 25]$  mm.

2. These two modes, which are also a mode pair, now contain vortices shedding asymmetrically, which is clear since the streamwise spatial modes are opposite in sign across the  $y = 0$  axis. The temporal spectra of all four of these modes show no distinct peaks, indicating the irregularity in the process. Interestingly, the frequency content in modes 1 and 2 is reminiscent of the frequency of vortex shedding behind a bluff body if we were to consider the space between the jets as the effective diameter of the bluff body. This behavior was also noted by Bunderson and Smith [15]. However, since we lack a clear peak in the spectra and have a non-zero velocity at the centerline inlet, we cannot confidently claim this is the case for our simulations.

DMD has been performed over the same region as the POD but over a much smaller subset of time of 0.01 seconds, or 101 snapshots. The dynamic modes (DM) that most closely correspond to the behavior found in the first four modes of the POD are shown in Figure 6a, along with the eigenvalue spectrum in Figure 6b. The complex eigenvalues come as conjugate pairs, so we only visualize the dynamic modes that correspond to the positive imaginary component of  $\mu$  to

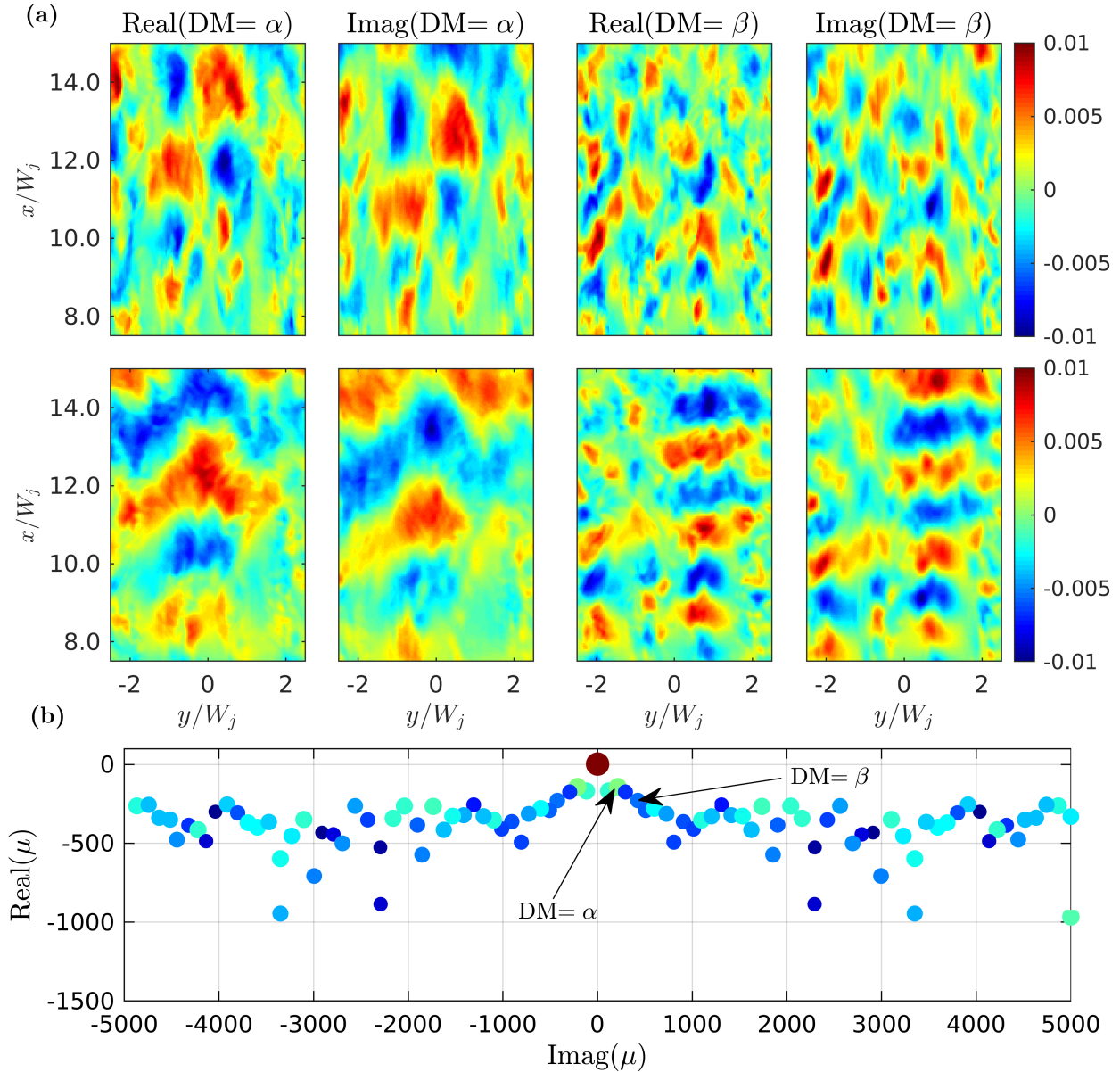


**Fig. 6 DMD (a) spatial modes for the streamwise and transverse velocity components in rows 1 and 2 and (b) eigenvalues computed for  $x \in [75, 150]$  mm and  $y \in [-25, 25]$  mm over a time frame of 0.01 seconds. The modes shown here correspond to eigenvalues with frequencies of  $\text{Imag}(\mu_\alpha) = 213$  Hz and  $\text{Imag}(\mu_\beta) = 425$  Hz.**

avoid repetitive information. In particular, these modes correspond to eigenvalues with frequencies of  $\text{Imag}(\mu_\alpha) = 213$  Hz and  $\text{Imag}(\mu_\beta) = 425$  Hz.

Interestingly, these two particularly dynamic modes resemble the same features in the POD modes and are also harmonics of each other. Yet, the two vortex shedding mechanics are different, one a result of symmetric shear layer roll-up and the other the result of asymmetric vortex shedding. This raises the question of whether it is the case that, once the shear layers begin to interact, they simply create vortex pairs that become asymmetric. We duly note that to find a portion of the flow in which these structures are clear took a tremendous effort. We trace this difficulty back to the fact that since dynamic modes are spectrally pure, the oscillations in the time frame must remain at a particular frequency for the entire time duration. As shown with POD, the vortex shedding is highly irregular, so finding this particular time frame of steadiness can be difficult.

## V. Conclusion

Two turbulent plane parallel interacting jets have been investigated using highly resolved simulations. Resolution between the three simulations was used by varying the maximum levels of AMR refinement. The time-average and RMS profiles were very similar between all three simulations, except in some cases because of the lack of available number of time steps of the finest resolution simulation.

Using POD and DMD modal decompositions, we examined the dynamical features that exist as the jets begin to interact. Through POD, we could identify a region in which the coherent structures originally shed vortices symmetrically, as single jets typically do, then the vortices begin shedding asymmetrically farther downstream. This transition process is highly irregular as indicated by the spectra of the temporal coefficients. DMD further confirmed this intermittent behavior, but also indicated that these oscillations can be captured in a single complex eigenvalue.

There are many avenues for improving this work in the future. First, we would like to confirm our turbulence generating process with experimental turbulence generating processes to validate our methodology. Second, we would like to ensure validity in our results by recomputing our higher resolution simulation for a longer duration and confirm the results discussed above. Finally, we would like to answer the question, “How does varying inlet turbulence intensity affect this process?” By answering this question, we can better understand the dynamics that occur as jets begin to interact.

## References

- [1] Bayly, B. J., Orszag, S. A., and Herbert, T., “Instability mechanisms in shear-flow transition,” *Annual Review of Fluid Mechanics*, Vol. 20, No. 1, 1988, pp. 359–391.
- [2] Winant, C. D., and Browand, F. K., “Vortex pairing: the mechanism of turbulent mixing-layer growth at moderate Reynolds number,” *Journal of Fluid Mechanics*, Vol. 63, No. 2, 1974, pp. 237–255.
- [3] Crow, S. C., and Champagne, F., “Orderly structure in jet turbulence,” *Journal of Fluid Mechanics*, Vol. 48, No. 3, 1971, pp. 547–591.
- [4] Diez, F. J., and Dahm, W. J., “Effects of heat release on turbulent shear flows. Part 3. Buoyancy effects due to heat release in jets and plumes,” *Journal of Fluid Mechanics*, Vol. 575, 2007, pp. 221–255.
- [5] Ball, C., Fellouah, H., and Pollard, A., “The flow field in turbulent round free jets,” *Progress in Aerospace Sciences*, Vol. 50, 2012, pp. 1–26.
- [6] Hussain, A., and Zedan, M., “Effects of the initial condition on the axisymmetric free shear layer: Effect of the initial fluctuation level,” *Physics of Fluids*, Vol. 21, No. 9, 1978, pp. 1475–1481.
- [7] Bogey, C., and Bailly, C., “Influence of nozzle-exit boundary-layer conditions on the flow and acoustic fields of initially laminar jets,” *Journal of Fluid Mechanics*, Vol. 663, 2010, pp. 507–538.
- [8] Brès, G. A., Jordan, P., Jaunet, V., Le Rallic, M., Cavalieri, A. V., Towne, A., Lele, S. K., Colonius, T., and Schmidt, O. T., “Importance of the nozzle-exit boundary-layer state in subsonic turbulent jets,” *Journal of Fluid Mechanics*, Vol. 851, 2018, pp. 83–124.
- [9] Stanley, S., and Sarkar, S., “Influence of nozzle conditions and discrete forcing on turbulent planar jets,” *AIAA journal*, Vol. 38, No. 9, 2000, pp. 1615–1623.
- [10] Ko, N., and Lau, K., “Flow structures in initial region of two interacting parallel plane jets,” *Experimental Thermal and Fluid Science*, Vol. 2, No. 4, 1989, pp. 431–449.
- [11] Nasr, A., and Lai, J., “Two parallel plane jets: mean flow and effects of acoustic excitation,” *Experiments in Fluids*, Vol. 22, No. 3, 1997, pp. 251–260.
- [12] Durve, A., Patwardhan, A. W., Banarjee, I., Padmakumar, G., and Vaidyanathan, G., “Numerical investigation of mixing in parallel jets,” *Nuclear Engineering and Design*, Vol. 242, 2012, pp. 78–90.
- [13] Yin, Z.-q., Zhang, H.-j., and Lin, J.-Z., “Experimental study on the flow field characteristics in the mixing region of twin jets,” *Journal of Hydrodynamics*, Vol. 19, No. 3, 2007, pp. 309–313.
- [14] Wang, H., Lee, S., and Hassan, Y. A., “Particle image velocimetry measurements of the flow in the converging region of two parallel jets,” *Nuclear Engineering and Design*, Vol. 306, 2016, pp. 89–97.

- [15] Bunderson, N. E., and Smith, B. L., "Passive mixing control of plane parallel jets," *Experiments in Fluids*, Vol. 39, No. 1, 2005, pp. 66–74.
- [16] Fujisawa, N., Nakamura, K., and Srinivas, K., "Interaction of two parallel plane jets of different velocities," *Journal of Visualization*, Vol. 7, No. 2, 2004, pp. 135–142.
- [17] Tyagi, A., Boxx, I., Peluso, S., and O'Connor, J., "The role of flow interaction in flame–flame interaction events in a dual burner experiment," *Proceedings of the Combustion Institute*, 2018.
- [18] Böhm, B., Stein, O., Kempf, A., and Dreizler, A., "In-nozzle measurements of a turbulent opposed jet using PIV," *Flow, Turbulence and Combustion*, Vol. 85, No. 1, 2010, pp. 73–93.
- [19] Stein, O. T., Böhm, B., Dreizler, A., and Kempf, A. M., "Highly-resolved LES and PIV analysis of isothermal turbulent opposed jets for combustion applications," *Flow, Turbulence and Combustion*, Vol. 87, No. 2-3, 2011, pp. 425–447.
- [20] Rieth, M., Proch, F., Stein, O., Pettit, M., and Kempf, A., "Comparison of the Sigma and Smagorinsky LES models for grid generated turbulence and a channel flow," *Computers & Fluids*, Vol. 99, 2014, pp. 172–181.
- [21] Anderson, E. A., and Spall, R. E., "Experimental and numerical investigation of two-dimensional parallel jets," *Journal of Fluids Engineering*, Vol. 123, No. 2, 2001, pp. 401–406.
- [22] Lin, Y., and Sheu, M., "Interaction of parallel turbulent plane jets," *AIAA Journal*, Vol. 29, No. 9, 1991, pp. 1372–1373.
- [23] Ghahremanian, S., Svensson, K., Tummers, M. J., and Moshfegh, B., "Near-field development of a row of round jets at low Reynolds numbers," *Experiments in Fluids*, Vol. 55, No. 8, 2014, p. 1789.
- [24] Suyambazhahan, S., Das, S. K., and Sundararajan, T., "Numerical study of flow and thermal oscillations in buoyant twin jets," *International Communications in Heat and Mass Transfer*, Vol. 34, No. 2, 2007, pp. 248–258.
- [25] Taira, K., Brunton, S. L., Dawson, S. T., Rowley, C. W., Colonius, T., McKeon, B. J., Schmidt, O. T., Gordeyev, S., Theofilis, V., and Ukeiley, L. S., "Modal analysis of fluid flows: An overview," *AIAA Journal*, 2017, pp. 1–29.
- [26] Lumley, J. L., "The structure of inhomogeneous turbulent flows," *Atmospheric Turbulence and Radio Wave Propagation*, 1967.
- [27] Holmes, P., Lumley, J. L., Berkooz, G., and Rowley, C. W., *Turbulence, coherent structures, dynamical systems and symmetry*, Cambridge university press, 2012.
- [28] Berkooz, G., Holmes, P., and Lumley, J. L., "The proper orthogonal decomposition in the analysis of turbulent flows," *Annual Review of Fluid Mechanics*, Vol. 25, No. 1, 1993, pp. 539–575.
- [29] Kerschen, G., Golinval, J.-C., Vakakis, A. F., and Bergman, L. A., "The method of proper orthogonal decomposition for dynamical characterization and order reduction of mechanical systems: an overview," *Nonlinear Dynamics*, Vol. 41, No. 1-3, 2005, pp. 147–169.
- [30] Schmid, P. J., "Dynamic mode decomposition of numerical and experimental data," *Journal of Fluid Mechanics*, Vol. 656, 2010, pp. 5–28.
- [31] Nonaka, A., Day, M. S., and Bell, J. B., "A conservative, thermodynamically consistent numerical approach for low Mach number combustion. Part I: Single-level integration," *Combustion Theory and Modelling*, Vol. 22, No. 1, 2018, pp. 156–184.
- [32] Rehm, R. G., and Baum, H. R., "The equations of motion for thermally driven, buoyant flows," *Journal of Research of the NBS*, Vol. 83, No. 297-308, 1978, p. 2.
- [33] Majda, A., and Sethian, J., "The derivation and numerical solution of the equations for zero Mach number combustion," *Combustion Science and Technology*, Vol. 42, No. 3-4, 1985, pp. 185–205.
- [34] Day, M. S., and Bell, J. B., "Numerical simulation of laminar reacting flows with complex chemistry," *Combustion Theory and Modelling*, Vol. 4, No. 4, 2000, pp. 535–556.
- [35] Dutt, A., Greengard, L., and Rokhlin, V., "Spectral deferred correction methods for ordinary differential equations," *BIT Numerical Mathematics*, Vol. 40, No. 2, 2000, pp. 241–266.
- [36] Minion, M. L., "A projection method for locally refined grids," *Journal of Computational Physics*, Vol. 127, No. 1, 1996, pp. 158–178.

- [37] Almgren, A. S., Bell, J. B., Colella, P., Howell, L. H., and Welcome, M. L., “A conservative adaptive projection method for the variable density incompressible Navier–Stokes equations,” *Journal of Computational Physics*, Vol. 142, No. 1, 1998, pp. 1–46.
- [38] Sirovich, L., “Turbulence and the dynamics of coherent structures. I, II, III. Coherent structures,” *Quarterly of Applied Mathematics*, Vol. 45, No. 3, 1987, pp. 561–571.
- [39] Rowley, C. W., Mezić, I., Bagheri, S., Schlatter, P., and Henningson, D. S., “Spectral analysis of nonlinear flows,” *Journal of Fluid Mechanics*, Vol. 641, 2009, pp. 115–127.
- [40] Kutz, J., Erichson, N., Askham, T., Pendergrass, S., and Brunton, S., “Dynamic Mode Decomposition for Background Modeling,” 2017.